Digital-holography efficiency measurements using a heterodyne-pulsed configuration

Steven A. Owens,[a,]* Mark F. Spencer[a,b] and Glen P. Perram[a]

[a]Air Force Institute of Technology, Department of Engineering Physics, Wright-Patterson
Air Force Base, Ohio, United States
[b]Directed Energy Directorate, Air Force Research Laboratory, Kirtland Air Force Base,
New Mexico, United States

Abstract. A digital-holography (DH) system is created in a heterodyne-pulsed configuration, meaning that the reference and signal pulses are nondeterministically correlated in time. Using the off-axis image plane recording geometry, two performance metrics are measured: (1) the total-system efficiency and (2) the ambiguity efficiency. These metrics are compared against the same measured efficiencies for a DH system in a homodyne-pulsed configuration, which uses deterministically correlated reference and signal pulses. The total-system efficiency of both systems is found to be consistent with one another, showing that no new component efficiencies are required when switching from a homodyne- to a heterodyne-pulsed configuration. Additionally, an instantaneous phase modulation model is used to characterize system performance in terms of nonideal pulse overlap. Such a model validates the use of the ambiguity efficiency for future efforts. © *The Authors. Published by SPIE under a Creative Commons Attribution 4.0 International License. Distribution or reproduction of this work in whole or in part requires full attribution of the original publication, including its DOI.* [DOI: 10.1117/1.OE.61.12.123101]

1 Introduction

Digital-holography (DH) systems can be designed to operate in long-range imaging scenarios that give rise to low-light and deep-turbulence conditions.[1–5] Such systems involve the digitization of a spatial-modulation pattern or "hologram" created via the interference of two fields of light.[6] These fields are referred to here as the reference and signal. From the recorded digital hologram, an estimate of the complex-optical field can be made, which in terms of amplitude and wrapped phase contains information about the aberrations that are distributed along the propagation path. Therefore, researchers are currently studying ways to improve long-range imaging performance using DH systems.[7–12]

The signal-to-noise ratio (SNR) is a key performance metric in terms of understanding the limitations of DH systems. This understanding requires the quantification of individual sources of SNR loss, otherwise known as efficiencies. The efficiencies of DH systems using continuous-wave (CW) laser sources have been extensively studied,[13–17] and the success of these systems is largely due to the long coherence lengths of modern-day CW laser sources. Nevertheless, as the path-length differences between the signal and reference exceed the coherence length of the CW laser source, system performance degrades rapidly.[14,15] This outcome says that the effective ranges of DH systems in a CW configuration is limited by longitudinal coherence.

Using pulsed laser sources with DH systems circumvent the limitations associated with the coherence length of CW laser sources, allowing for longer effective ranges. Even so, pulsed laser sources introduce additional considerations, such as the temporal overlap of the fields of light being interfered. To this end, the effect of temporal delay between the reference and signal pulses was recently studied using a 1064-nm pulsed laser source and a short-wave infrared (SWIR) camera.[18] These experiments showed that the measured total-system efficiency was comparable to that of a DH system in a CW configuration. It also introduced a novel component efficiency,

---

called the ambiguity efficiency, to capture the effects of reduced pulse overlap. With the outcomes of Ref. 18 in mind, more research is still required to fully characterize DH systems in a pulsed configuration. In response, this paper presents two-novel contributions to expand the understanding of such systems.

The first novel contribution leverages previous work and studies a fundamentally different pulsed configuration. In the previous work, the signal and reference pulses were deterministically correlated, since a postamplification beam splitter was used to create the two fields of light being interfered from a single-pulse train.[18] This idealization isolated the effect of reduced pulse overlap by ensuring the temporal characteristics of the reference and signal pulses were identical before interaction with the experiment. Thus this previous configuration is referred to as the "homodyne-pulsed configuration" throughout this paper.

In this paper, system performance is analyzed using signal and reference pulses with non-identical temporal characteristics. This new configuration is referred to as the "heterodyne-pulsed configuration" throughout this paper. By eliminating the identical-field constraint, the heterodyne-pulsed configuration increases the applicability of DH systems, especially for long-range imaging scenarios.[1–5] For instance, a preamplification beam splitter can be used to create the signal and reference pulses from two-independent pulse trains, allowing for stronger signal pulses and greater effective ranges. That or a single-pulse train can be used with one pulse being one field and a subsequent pulse being the other. In both cases, the effective strengths of the pulses can be set within the dynamic range of the camera, and the timing of the pulses can be externally triggered to maximize pulse overlap.

In support of the first novel contribution, this paper measures the total-system efficiency. In so doing, the results show that the measured total-system efficiency of a heterodyne-pulsed configuration is consistent with that of a homodyne-pulsed configuration. As such, no new component efficiencies, which make up the total-system efficiency, are required to characterize system performance.

The second novel contribution shows that the ambiguity efficiency sufficiently accounts for nonideal pulse overlap. In Ref. 18, the predicted ambiguity efficiency matched the measured ambiguity efficiency well only when the temporal delay between the reference and signal pulses was small. For large temporal delays, the model over predicted system performance. Multiple potential reasons were given in Ref. 18, but none were explored in depth. As a result, a more sophisticated and accurate model was formulated, specifically for the homodyne-pulsed configuration, and presented in a recent conference proceeding.[19]

In support of the second contribution, this paper significantly adapts the model presented in Ref. 19, specifically for the heterodyne-pulsed configuration, and analyzes the effect of an instantaneous phase modulation. A phase modulation could result from many issues within the laser source but the effect on the ambiguity efficiency will be the same. Therefore, this paper investigates an instantaneous carrier frequency change or "mode hop" within the fields of light being interfered. The ambiguity efficiency is predicted for simple heterodyne fields both with and without a mode hop included in the model. Overall, the results show that this model leads to a more accurate ambiguity efficiency prediction. Therefore, the ambiguity efficiency sufficiently accounts for nonideal pulse overlap.

In what follows, this paper begins with a review of the applicable efficiencies in Sec. 2. Section 3 then details the experiment, including the data-collection and data-processing methodologies. The results from the experiment and the effect of an instantaneous phase modulation are presented in Sec. 4, and a succinct summary of these results concludes this paper in Sec. 5. Two appendices then follow to capture pertinent discussions that are not critical to understanding the two-novel contributions of this paper.

2 Theory

Although multiple DH recording geometries exist,[1–4,17] the off-axis image plane recording geometry (IPRG) was used in this paper because of its simplicity in setup.[1,11–19] For the off-axis IPRG, light from a master oscillator is split into two optical paths. One optical path scatters light off an optically rough, extended object. The scattered signal is collected by the pupil of an imaging

system to create the signal field U_S and imaged onto the focal plane array (FPA) of a camera. The other optical path creates a reference field U_R by flood illuminating the FPA. The strong reference is injected off axis, relative to the pupil, via a local oscillator (LO).

In conjunction with the off-axis IPRG, this paper uses the power definition of the SNR,[1,3] such that

$$\mathrm{SNR}(x, y, \tau) = \eta_{\mathrm{tot}}(x, y, \tau) \frac{4q_I^2}{\pi} \overline{m}_S(x, y), \tag{1}$$

where (x, y) are the estimated image-plane coordinates, τ is the temporal delay between the centers of the reference and signal pulses, η_{tot} is the total-system efficiency, q_I is the image-plane sampling quotient, and $\overline{m}_S$ is the mean number of signal photoelectrons generated by the signal pulse. It should be noted that Eq. (1) assumes the reference is sufficiently strong such that the noise in the reference pulse dominates all other noise sources. In other words, Eq. (1) says that the DH system is operating in a shot-noise-limited regime.[3,16] However, if the DH system is not operating at the shot-noise limit, all detrimental effects are captured by η_{tot} and Eq. (1) remains valid.

Analyzing η_{tot} more closely, the total-system efficiency is the product of many independent sources of SNR degradation such that[13,18]

$$\eta_{\mathrm{tot}}(x, y, \tau) = \eta_{\mathrm{ern}}(x, y)\eta_{\mathrm{snl}}(x, y)\eta_{\mathrm{mix}}(x, y, \tau), \tag{2}$$

where η_{ern} is the excess-reference-noise efficiency, η_{snl} is the shot-noise-limit efficiency, and η_{mix} is the mixing efficiency. The excess-reference-noise efficiency quantifies the spatial uniformity of the reference field, and the shot-noise-limit efficiency quantifies the strong-reference approximation made in Eq. (1). Both efficiencies are described in detail elsewhere[13,16,18] and are not of primary concern in this paper.

The mixing efficiency, however, merits additional consideration, since it quantifies of how well the reference and signal pulses interfere. In general,

$$\eta_{\mathrm{mix}}(x, y, \tau) = \eta_{\mathrm{pol}}(x, y)\eta_{\mathrm{mod}}(x, y)\eta_{\mathrm{amb}}(\tau), \tag{3}$$

where η_{pol} is the polarization efficiency,[13] η_{mod} is the modulation efficiency,[17] and η_{amb} is the ambiguity efficiency.[18] The polarization efficiency is the quantification of how well the polarization axes of the reference and signal pulses align, and the modulation efficiency is a quantification of how well the finite pixels of the FPA record the continuous hologram. As with η_{ern} and η_{snl}, η_{pol} and η_{mod} are discussed in detail elsewhere[13,17,18] and are not of primary concern in this paper.

In contrast, η_{amb} is a main focus of this paper as it is the only efficiency dependent on the temporal overlap between the reference and signal pulses. The ambiguity efficiency is derived from the zero-Doppler cut of the ambiguity function,[20–22] such that

$$\eta_{\mathrm{amb}}(\tau) = \left\langle \left| \int_{-\infty}^{\infty} U_R(x, y, t) U_S^*(x, y, t - \tau) \mathrm{d}t \right|^2 \right\rangle$$
$$= \left\langle \left| \int_{-\infty}^{\infty} \tilde{U}_R^*(x, y, \nu) \tilde{U}_S(x, y, \nu) e^{-j2\pi\nu\tau} \mathrm{d}\nu \right|^2 \right\rangle, \tag{4}$$

where U_R and U_S are the complex-optical fields of the reference and signal pulses in the temporal domain, respectively, t is the time, $\tilde{U}_R$ and $\tilde{U}_S$ are the complex-optical fields of the reference and signal pulses in the spectral domain, respectively, ν is the frequency, $*$ denotes the complex conjugate, $|\bullet|^2$ is the square-magnitude operator, and $\langle \bullet \rangle$ is the spatial average operator. The square magnitude operator is necessary as, again, Eq. (1) uses the power definition for SNR. The spatial average operator is not required in Eq. (4), but it is convenient to have spatially independent metrics when cross evaluating multiple DH systems and is thus used here. For this reason, all modeled efficiencies are assumed to be spatially uniform and the spatial dependencies of Eqs. (1)–(3) are henceforth dropped.
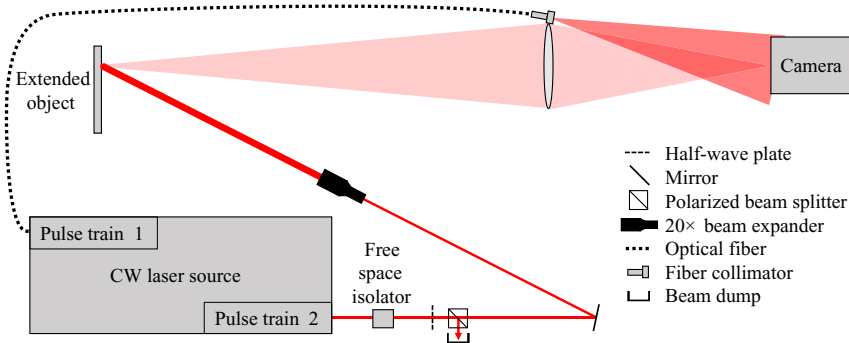
Fig. 1 Experimental setup overview.

3 Experiment

As shown in Fig. 1, a DH system was set up with a 1064-nm pulsed laser source and a SWIR camera in the off-axis IPRG. The laser source was a custom-built NP photonics coherent high-energy pulsed fiber laser system.[23] This laser source was set up in a heterodyne-pulsed configuration, such that the signal and reference pulses were created from two-independent pulse trains in a master oscillator power amplifier or "MOPA" configuration. In practice, other heterodyne-pulsed configurations exist, but the conclusions reached in this paper hold for them as well.

To create the two-independent pulse trains, a preamplification beam splitter was used after the CW seed laser (i.e., master oscillator) with a 1064-nm center wavelength. After the beam splitter, each beam was independently intensity modulated then amplified via independent ytterbium-doped fiber amplifier stages. The independence of the intensity modulation and amplification stages is the fundamental difference between the heterodyne experiment presented here and the homodyne experiment presented in Ref. 18. Both pulse trains produced pulses at a 1-kHz repetition rate. Beam diagnostics were measured via beam-path insertion and, when applicable, within the dynamic range of the diagnostic tool.

Pulse train 1 produced 8.8 ns pulses with an average energy of 10 nJ. The resulting reference pulses exited the backend tip of a 2-m-long polarization–maintaining, single-mode optical fiber. The backend tip was placed off axis next to the imagining lens and tilted toward the camera. An adjustable collimator was also used to ensure enough energy from the reference pulses was captured by the camera while maintaining a nearly uniform energy distribution over the camera's FPA.

Pulse train 2, on the other hand, produced 10 ns pulses with an average energy of 10 μJ. The resulting signal pulses passed through a free-space isolator, half-wave plate, and polarized beam splitter (PBS). The half-wave plate and PBS were used to control the energy of the signal pulses to avoid camera-pixel saturation, as discussed later. After the PBS, the signal pulses were sent through a 20× beam expander, resulting in an approximate beam size of 4 cm. The expanded beam was scattered off a sheet of Labsphere Spectralon (i.e., the stationary, optically rough, extended object) with a vendor-specified 99% Lambertian reflectivity, and imaged onto the camera via a 2.54-cm imaging lens. It should be noted that the object and image distances were set such that the measured image-plane sampling quotient q_I was 3.35.[1,3] By definition, q_I represents the number of circular-pupil diameters that can fit across the Fourier plane.

The spectral line shapes of the reference and signal pulses were measured using a Thorlabs SA200-8B scanning Fabry–Perot interferometer with a 7.5-MHz resolution and 1.5-GHz free spectral range and are shown in Fig. 2,[24,25] respectively.

It was evident from the line shapes shown in Fig. 2 that the two-independent pulse trains were operating suboptimally. For example, at least two modes were visible in both line shapes. Subsequent spatial beam profile measurements confirmed the multimode nature of the pulses.[18] Analysis showed the larger of the two modes in each line shape, or the fundamental mode, was consistent with a Laguerre–Gauss ($p = 0$, $l = 0$) mode. Furthermore, the smaller of the two modes, or the secondary mode, was consistent with a Laguerre–Gauss ($p = 1$, $l = 0$) mode. From the laser construction parameters, the total spacing between these two modes was
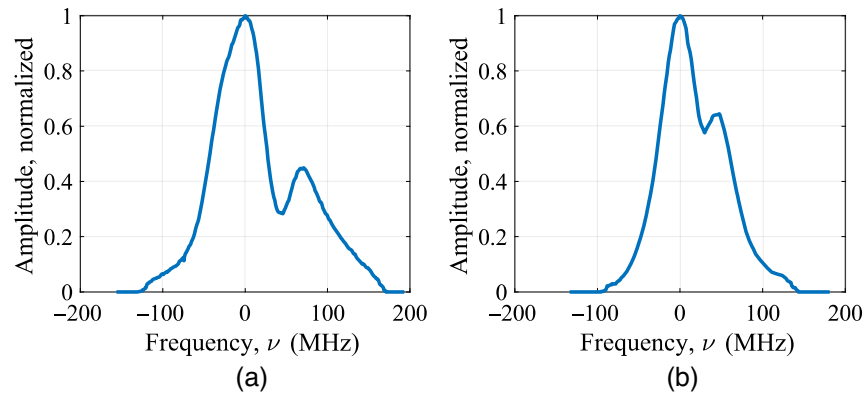
Fig. 2 Spectral line shapes of the (a) reference and (b) signal pulses.

determined to be on the order of 1.5 GHz.[18,23] This outcome means one mode had been aliased onto the other due to the limitations of the Fabry–Perot interferometer.

In addition to multimode operation, the line shapes and widths in Fig. 2 were not consistent with Fourier-transform limited pulses. This outcome, paired with differences in mode shape, width, and relative spacing for the reference and signal line shapes, indicated that the pulse shaping and amplification processes were negatively affecting the line shapes in different ways. These differences may have been caused by a myriad of reasons, including unequal dispersion along independent propagation paths or nonuniform spatial sampling within the gain media.

The average energy from the two-independent pulse trains fluctuated $\pm 16\%$ pulse to pulse consistently over a 6-h time period, over twice as long as required to collect all necessary data. Therefore, the energy in each pulse was considered stable. The temporal overlap between the reference and signal pulses at the camera FPA was controlled during the intensity modulation process using a Berkeley Nucleonics Corporation Model 577 Digital Delay/Pulse Generator. This experimental nob allowed the total-system efficiency to be measured as a function of relative pulse delay τ with a minimum sampling resolution of 250 ps and a root-mean-squared jitter of 100 ps. All optical elements used in the experimental setup were either achromatic or coated to maximize transmission or reflection.

The camera was an Allied Vision Goldeye G-033 SWIR TEC1, exhibiting a pixel-well depth of 25,000 photoelectrons (pe), a quantum efficiency of 77% at 1064 nm, and an array size of 512×640 at a 15-μm pixel pitch. This camera also had a measured unstable gain region for integration times <25 μs, resulting in over a quarter of the pixel-well depth being filled by dark-current noise. In turn, the dark-current noise was the dominant factor in the camera-noise variance σ_n^2. Overall, $\sigma_n^2 = 6419$ pe^2. Due to the unstable gain region, the experiment was set up for the reference and signal pulses to arrive near the 27-μs integration-time mark with a total frame-integration time of 30 μs.

Because of the high-dark-current noise, the mean number of photoelectrons generated by the reference and signal pulses, $\overline{m}_R$ and $\overline{m}_S$ respectively, were set to $\overline{m}_R = 11,449$ pe and $\overline{m}_S = 77$ pe to avoid camera-pixel saturation, yet maximize sensing. Assuming Poisson statistics, where the mean is equal the variance, this outcome meant the reference pulses did not dominate all noise sources, as $\sigma_n^2 > 1/2\overline{m}_R$. Therefore, the DH system used in this experiment was not operating in the shot-noise-limited regime.[3,16] As a reminder, this shortcoming was accounted for by the shot-noise-limit efficiency η_{snl} [see Eq. (2)]. For the system presented above, $\eta_{\mathrm{snl}} = 81\%$.

3.1 Data-Collection Methodology

Digital holograms were collected for temporal pulse delay values from $\tau = -5.875$ ns to $+6.125$ ns in 1 ns increments and from $\tau = -1.875$ to $+2.125$ ns in 0.25-ns increments to sufficiently sample both the wings and the peak of the total-system efficiency curve. Two measurements were taken at $\tau = 0$, one at the beginning of the overall data collection period and one at the halfway mark, to ensure the master oscillator and amplification paths were performing

consistently for all datasets. For each measurement increment, the Labsphere Spectralon sheet was rotated to generate 10 distinct speckle realizations. For each speckle realization, 10 digital-hologram frames were collected for a total of 100 digital-hologram frames for each temporal pulse delay value. This was done for speckle averaging during data processing. Additionally, 10 reference-only frames and 10 signal-only frames were collected for each speckle realization during both $\tau = 0$ measurements. Reference-only and signal-only frames were unnecessary for all temporal delay values because the energy of both pulse trains was considered stable. After all frames were collected, 100 background frames were collected so the background and camera noise could be appropriately accounted for during efficiency calculations. All frames were imported to MATLAB for processing.

3.2 Data-Processing Methodology

To calculate the total-system and ambiguity efficiencies, the collected frames were first demodulated. An example using a digital-hologram frame is shown in Fig. 3.

For the example provided, a discrete inverse Fourier transform was performed on the real-valued digital hologram in Fig. 3(a) to obtain the associated complex-valued Fourier plane in Fig. 3(b). The Fourier plane, in accordance with the off-axis IPRG,[1,3] contained four important terms as follows:

(1) the signal field (the data in the top-right circular pupil);
(2) the complex-conjugate of the signal field (the data in the bottom-left circular pupil);
(3) the LO-autocorrelation (the noncircularly symmetric data centered at DC); and
(4) the pupil-autocorrelation (the circularly symmetric data centered at DC).

Given (1)–(4), a pupil-filter function was used to filter the desired signal field term. The filtered data were then centered in the Fourier plane before undergoing a discrete Fourier transform to obtain the associated complex-valued image plane in Fig. 3(c), concluding frame demodulation.

Each collected frame underwent frame demodulation individually. Otherwise, the piston-phase mismatch introduced on a frame-to-frame basis by the two-independent pulse trains may have washed out the spatial modulation pattern of the digitized hologram, artificially reducing measured SNR. Once the individual frames were demodulated, the energy, or square-magnitude, of each demodulated frame was calculated in pe^2 in accordance with the power definition of SNR [see Eq. (1)]. The mean of all 100 demodulated energy frames was computed for each pulse delay increment τ to produce an average demodulated energy frame. Frame demodulation and the average demodulated energy frame calculation was repeated for the collected reference-only, signal-only, and background frames using the same pupil-filter function as was used for the digital-hologram frames. This ensured the noise collected with the digital-hologram frames was appropriately accounted for during calculations.

Using the calculated average demodulated energy frames, the measured total-system efficiency η'_{tot} was computed using the following equations:
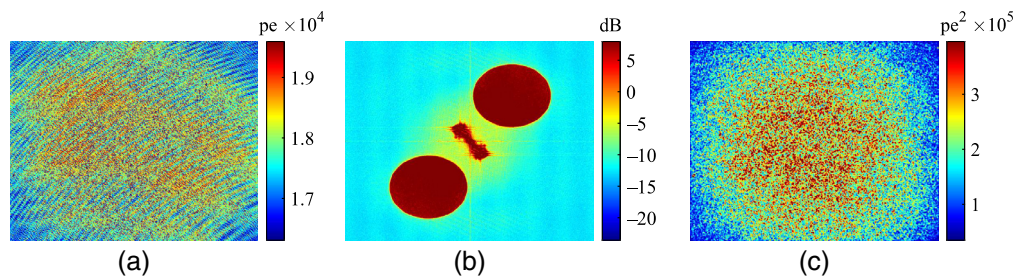
Fig. 3 Frame-demodulation example using a digital-hologram frame. The demodulation process involves (a) the recorded frame, (b) the associated Fourier plane, and (c) the associated image frame.

$$E'_N(x, y) = E'_{D-R}(x, y) + E'_{D-S}(x, y) - E'_{D-B}(x, y), \tag{5}$$

$$E'_H(x, y, \tau) = E'_{D-H}(x, y, \tau) - E'_N(x, y), \tag{6}$$

and

$$\eta'_{\text{tot}}(\tau) = \left\langle \frac{\text{SNR}'(x, y, \tau)}{\text{SNR}(x, y)} \right\rangle = \frac{\pi}{4q_I^2} \left\langle \frac{E'_H(x, y, \tau)/E'_N(x, y)}{\overline{m}'_S(x, y) - \overline{m}'_B(x, y)} \right\rangle, \tag{7}$$

where E'_N is the measured noise energy; E'_{D-R}, E'_{D-S}, and E'_{D-B} are the measured reference, signal, and background average energies after frame demodulation, respectively; E'_H is the measured hologram energy; E'_{D-H} is the measured hologram average energy after frame demodulation; SNR' is the measured SNR; and $\overline{m}'_S$ and $\overline{m}'_B$ are the measured mean number of signal and background photoelectrons generated, respectively. Note that the substantial dark-current noise from the camera is accounted for with $\overline{m}'_B$ and E'_{D-B} and is removed, where applicable, by background subtraction. It should also be noted that the $\pi/4q_I^2$ term in Eq. (7) is necessary to account for the ratio of the pupil-filter function area to the total Fourier plane area.[1,3] The spatial average operator was used to generate a convenient single-valued metric at a given τ, as was done for Eq. (4).

The measured ambiguity efficiency η'_{amb} follows as the amplitude normalization of the measured total-system efficiency. In particular,

$$\eta'_{\text{amb}}(\tau) = \frac{\eta'_{\text{tot}}(\tau)}{\eta'_{\text{tot}}(0)}. \tag{8}$$

This relationship ensures that η'_{amb} equals unity when the reference and signal fields are perfectly overlapped (i.e., $\tau = 0$ ns) and is always less than one otherwise.

4 Results

Using Eqs. (5)–(8), the measured total-system and ambiguity efficiencies for a DH system in a heterodyne-pulse configuration were calculated. To analyze the effects of using pulses with non-identical temporal characteristics, the measured efficiencies were compared to those of a DH system in a homodyne-pulsed configuration.[18] The total-system efficiencies at $\tau = 0$ ns were similar and well within the uncertainty of each measurement. Furthermore, the ambiguity efficiency curves exhibited the same general features. Therefore, it was concluded that a heterodyne-pulsed configuration is, in terms of performance, consistent with a homodyne-pulsed configuration. A potential reason for the discrepancies between the ambiguity efficiency predicted using Eq. (4) and the measured ambiguity efficiency for the heterodyne-pulsed configuration was then investigated using a complex-optical field model.

4.1 Comparison of Total-System Efficiency

Equations (5)–(7) were used to calculate a measured total-system efficiency at $\tau = 0$ ns of $13.5\% \pm 6.4\%$ for the DH system described in Sec. 3 with a heterodyne-pulsed configuration. This was 15% lower than the measured total-system efficiency at $\tau = 0$ ns of $15.9\% \pm 10.3\%$ for the DH system used in Ref. 18 with a homodyne-pulsed configuration, but the uncertainty bounds of both measurements were well overlapped. Also the decrease in total-system efficiency for the heterodyne-pulsed configuration was most likely caused by the temporally shorter reference pulse. An 8.8-ns pulse was used for the reference pulse in the heterodyne experiment, whereas a 10-ns pulse was used in the homodyne experiment. This meant that the interaction time between the fields was shorter and the amplitudes in which that interaction occurred were reduced for the heterodyne experiment. Therefore, the decrease in system performance for the heterodyne-pulsed configuration can be attributed to the design of this specific experiment, not the use of a heterodyne-pulsed configuration in general.
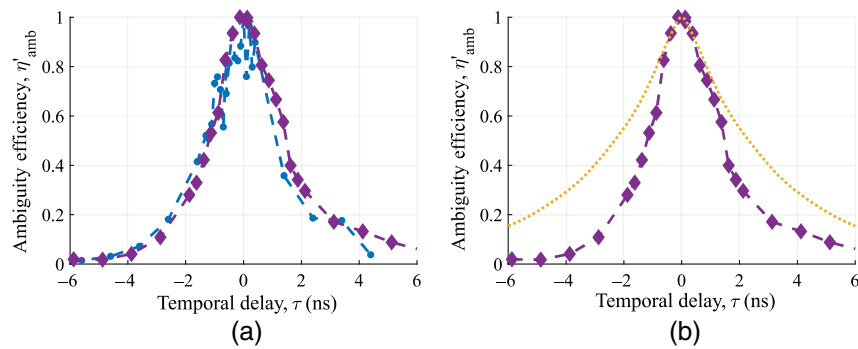
Fig. 4 Comparison between the measured ambiguity efficiency for the heterodyne-pulsed configuration (- ♦) and (a) the measured ambiguity efficiency for the homodyne-pulsed configuration (- •) from Ref. 18 and (b) the predicted ambiguity efficiency for the heterodyne system (···).

With the measured total-system efficiency of both systems calculated for $\tau = 0$ ns, it was sufficient to make all further comparisons between the configurations using their respective ambiguity efficiencies. This ensured any additional differences in system performance would not be attributed to the shortened reference pulses used in the heterodyne experiment. The measured ambiguity efficiencies for the heterodyne- and homodyne-pulsed configurations, as well as the ambiguity efficiency predicted for the heterodyne experiment using Eq. (4), are shown in Fig. 4.

In Fig. 4(a), the ambiguity efficiencies for the two configurations are well overlapped. Both follow the same general shape, including the width of each curve and the asymmetry about $\tau = 0$ ns. The ambiguity efficiency for the homodyne-pulsed configuration for $|\tau| \leq 2$ ns was more erratic than that of the heterodyne-pulsed configuration because of the measurement technique used in Ref. 18. Specifically, the reference and signal quantities used in Eqs. (5)–(7) were calculated at each increment of τ. The pulse-to-pulse energy fluctuations in the laser source led to a higher degree of variation between adjacent-τ measurements. Such variation was avoided in the heterodyne-pulsed configuration by only measuring the reference and signal quantities required in Eqs. (5)–(7) at $\tau = 0$ ns. This outcome was possible because the reference, and signal pulses were stable in energy (see Sec. 3). These similarly shaped ambiguity efficiency curves, along with the consistent total-system efficiencies at $\tau = 0$ ns, indicated there was no significant difference in performance when using either a heterodyne- or homodyne-pulsed configuration. Additionally, there were no efficiencies introduced by a heterodyne-pulsed configuration that had not already been accounted for in the previous research. Therefore, in terms of system performance, homodyne- and heterodyne-pulsed configurations are consistent.

The ambiguity efficiency predicted using Eq. (4), however, did not match the measured ambiguity efficiency calculated using Eq. (8), as seen in Fig. 4(b). The fields used as inputs to the spectral formulation shown in Eq. (4) (i.e., the lower term) were estimated from the line shapes shown in Fig. 2. First, a two-term Lorentzian profile was fit to each spectral line shape. The root-mean-squared error (RMSE) for the reference line shape was 4.7%, and the RMSE for the signal line shape was 3.5%. Then with the knowledge that the fundamental and secondary modes were spaced ~1.5 GHz apart (see Sec. 3), the frequency center of the secondary mode in both fitted Lorentzian profiles was shifted +1.5 GHz. These fitted, shifted Lorentzian profiles were then used as the field inputs to Eq. (4). An assumption that no interaction took place between fundamental and secondary modes was then made.[26] The resulting function was taken as the predicted ambiguity efficiency. A detailed explanation of this process can be found in Appendix B of Ref. 18.

In Fig. 4(b), the ambiguity efficiency was predicted accurately for $|\tau| \leq 1$ ns but was over-predicted for values $|\tau| \geq 1$ ns. As a result, the average percent error of the prediction was 149.45%. The most probable cause of this over prediction was inaccuracy of the input field estimates.[19] The aliasing and 7.5 MHz resolution of the Fabry–Perot interferometer could have smoothed or hid important features of the spectral line shapes, and certain operational characteristics would be unidentifiable from others. Either of these issues could have led to the inaccurately predicted ambiguity efficiency.

In line with these issues, a potential solution for the inaccurate ambiguity efficiency was postulated: instead of simultaneous propagation of multiple modes, the two-independent pulse trains each experienced an instantaneous phase modulation. It should be noted the effect of this potential solution on the predicted ambiguity efficiency is not unique. In other words, even if including a phase modulation in the input field estimates sufficiently narrows the ambiguity efficiency prediction, other potential solutions cannot be eliminated. Additionally, it is not a guarantee that a phase modulation is present in the fields. The following analysis was performed to validate Eq. (4) as a model for the ambiguity efficiency not to identify any nonideal characteristics of the laser used in this experiment. By showing it is possible to predict the observed ambiguity efficiency curve width and asymmetry, the ambiguity efficiency model was validated.

4.2 Validating the Ambiguity Efficiency Model

To investigate the effect on the ambiguity efficiency of including an instantaneous phase modulation in the input fields, a model for the complex-optical fields was created. For this model, it was assumed that the base reference and signal fields could be represented spectrally by pure, Fourier-transform-limited Lorentzian line shapes[27] for the temporal pulse parameters given in Sec. 3. This choice resulted in full-width half-maximums (FWHMs) of 50 MHz for the reference line shape and 44 MHz for the signal line shape. Each field was also assumed to have two modes spaced ~1.5 GHz apart, identical in all ways except amplitude. The amplitudes of each mode were set to best match the measured data shown in Fig. 2. For convenience, the fields described in this paragraph will be referred to as the ideal spectral fields for the remainder of this paper.

Once these ideal spectral fields were defined, they were converted to the temporal domain using a Fourier transform.[28] This was done to ease modeling and computation requirements. The temporal formulation for an instantaneous phase modulation was then multiplied to these ideal temporal fields independently, so the effects on the ambiguity efficiency could be analyzed. As a reminder, an instantaneous phase modulation can be caused by multiple issues, all of which result in the same ambiguity efficiency. Therefore, a mode hop was chosen for modeling simplicity. As such, the temporal fields were defined as

$$U_{R,S}(t) = \hat{U}_1^{R,S}(t)\xi_1(t) + \hat{U}_2^{R,S}(t)\xi_2(t), \tag{9}$$

and

$$\xi_1(t) = |1 - \xi_2(t)| = \begin{cases} 1, & t < t_0 \\ 0, & t \geq t_0 \end{cases}, \tag{10}$$

where the subscripts and superscripts R and S indicate the reference and signal fields, respectively, the subscripts 1 and 2 indicate the fundamental and secondary modes, respectively, ξ is the function for a mode hop, and t_0 is the time in which the mode hop occurs. Note the lack of spatial dependence in Eqs. (9) and (10). Preliminary analysis indicated including spatial dimensions would minimally affect the results. As such, the spatial dependence was removed to improve computation time. However, other potential solutions, especially ones investigating the effect of transverse decoherence, would require spatial dependence to be included in Eq. (9).

Before presenting the results concerning the validity of the ambiguity efficiency model presented in Eq. (4), a comment about the analysis is required. No effort to model the system hardware was made. Specifically, the measurement of a spectral line shape of a pulsed laser source using a Fabry–Perot interferometer was ignored.[24,25] Therefore, the model-based spectral line shapes reported below were not expected to match the measured line shapes well and were not a requirement for model validation.

For the instantaneous phase modulation analysis, it was assumed the phase modulation, as modeled by a mode hop, occurred in the amplification stages. To clarify, the intensity modulation scheme (i.e., pulse carving) would require the CW seed to experience a phase modulation every 10 ns on average if the phase modulation occurred in the CW seed. This outcome would be indicative of a level of instability not seen in the laser-beam performance. Therefore, the phase modulation must have taken place in the amplification stages. As a result, the relative mode
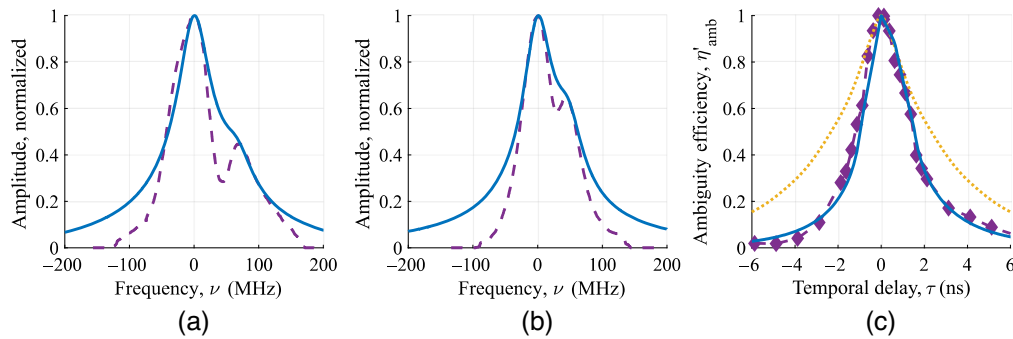
Fig. 5 Aliased spectral line shapes of (a) the reference field and (b) the signal field, and (c) the predicted ambiguity efficiency when including a phase modulation in the complex-optical field model. For all plots, the model results (–) are compared to the measured data (- - and - ♦). Additionally, the original ambiguity efficiency prediction (⋯) from Fig. 4(b) is included in (c).

amplitude and spacing were allowed to change independently in each line shape so that the field-model line shapes matched the measured line shapes as best as possible. With this and the other field-model parameters in mind, the predicted ambiguity efficiency was calculated by substituting Eqs. (9) and (10) into Eq. (4). The aliased spectral line shapes and predicted ambiguity efficiency are shown in Fig. 5.

As seen in Figs. 5(a) and 5(b), the spectral line shapes for the reference and signal fields when an instantaneous phase modulation is included in the field model do not match the measured spectra well. The widths of the fundamental peaks are roughly accurate. In contrast, for both modeled-field line shapes, the existence of a second mode is ambiguous and too much importance is given to the wings. However, these errors cannot be meaningfully improved if a single-phase modulation is the only imperfection considered, as was the case here. As a reminder, the line shapes calculated using the complex-optical field model were not linked to validation requirements for the ambiguity efficiency model.

The predicted ambiguity efficiency when including a phase modulation in the complex-optical field model was significantly narrowed, as shown in Fig. 5(c). The field model prediction was more accurate than the original prediction at all measured data points where $|\tau| \geq 1$ ns. Overall, the average percent error of the prediction was 21.03%, an 85.93% improvement over the prediction made without including the mode hop. Asymmetry was also introduced in the ambiguity efficiency prediction, nearly matching the asymmetry in the measured data. Because the inclusion of an instantaneous phase modulation produced a predicted ambiguity efficiency similar to the measured results, further validation of the model presented in Eq. (4) was indicated.

5 Conclusion

A DH system was created in a heterodyne-pulsed configuration. Using the off-axis IPRG, two performance metrics were measured: (1) the total-system efficiency and (2) the ambiguity efficiency. These metrics were compared against the same measured efficiencies for a DH system in a homodyne-pulsed configuration. The total-system efficiency of both systems was found to be consistent with one another, showing that no new component efficiencies were required when switching from a homodyne- to a heterodyne-pulsed configuration. Additionally, an instantaneous phase modulation model was used to characterize system performance in nonideal pulse overlap. Such a model validated the use of the ambiguity efficiency for future efforts.

6 Appendix A: Further Discussion on Cycloergodicity

It is worth noting that work has been performed to characterize the temporal coherence of pulsed laser sources and their associated effects.[29–33] At large, the underpinning theory, modeling and simulation, and experiments assumed cycloergodicity.[29–32] In other words, the pulses were temporally and spatially identical for all time, resulting in no frame-to-frame variations in the

recorded digital holograms. However, by definition, DH systems in a pulsed configuration do not satisfy the cycloergodicity condition. The nonidentical temporal characteristics, such as the phases or spectral content, of the reference and signal pulses lead to substantial variations in the in the recorded digital holograms. As a result, the second-order moment, or variance, of the associated pulses is nonzero.

Limited coherence theory has been developed for noncycloergodic pulses and relies on nearly incoherent sources and long integration times.[33] In contrast, DH systems in a pulsed configuration require partially coherent sources and nearly instantaneous measurements. Therefore, the work presented in this paper goes significantly past previous efforts and validates temporal-coherence theory for noncycloergodic pulses via the ambiguity efficiency.

7 Appendix B: Further Discussion on the Ambiguity Efficiency

Although the ambiguity efficiency captures the SNR degradation caused by temporal misalignment of the fields, caution must be taken when using Eq. (4) to predict DH system performance (specifically in a pulsed configuration). Measuring the temporal or spectral fields for optical wavelengths is nontrivial. Many common nonimaging optical measurement devices, such as fast photodiodes and Fabry–Perot interferometers, only directly measure irradiance. The field is then estimated from irradiance, meaning much of the wrapped phase information is lost. This loss could lead to important phase-related artifacts being hidden within the measurements. In turn, the ambiguity efficiency predictions made from these measurements are inaccurate. Typically, the ambiguity efficiency prediction will overestimate system performance.

One such phase-related artifact, an instantaneous phase modulation, is investigated in this paper. A phase modulation could be caused by many factors and is indistinguishable from simultaneous multimode propagation when using common frequency measurement devices such as, a Fabry–Perot interferometer. However, assuming the incorrect form of multimodal laser operation results in an inaccurate ambiguity efficiency prediction.

Acknowledgments

Data Availability

Data underlying the results presented in this paper are not publicly available at this time but may be obtained from the authors upon reasonable request.

References

1. M. F. Spencer et al., "Deep-turbulence wavefront sensing using digital-holographic detection in the off-axis image plane recording geometry," *Opt. Eng.* **56**(3), 031213 (2017).
2. M. T. Banet, M. F. Spencer, and R. A. Raynor, "Digital-holographic detection in the off-axis pupil plane recording geometry for deep-turbulence wavefront sensing," *App. Opt.* **57**(3), 465–475 (2018).
3. M. F. Spencer, "Spatial heterodyne," in *Encyclopedia of Modern Optics*, B. Guenther and D. Steel, 2nd ed., eds., Elsevier, Amsterdam, The Netherlands (2018).
4. D. E. Thornton, M. F. Spencer, and G. P. Perram, "Deep-turbulence wavefront sensing using digital holography in the on-axis phase shifting recording geometry with comparisons to the self-referencing interferometer," *App. Opt.* **58**(5), A179–A189 (2019).
5. M. F. Spencer, "Limitations of the deep-turbulence problem," in *Proc. OSA*, p. PW3F.1 (2021).

6. J. W. Goodman and R. W. Lawrence, "Digital image formation from electronically detected holograms," *App. Phys. Lett.* **11**(3), 77–79 (1967).

7. J. C. Marron and K. S. Schroeder, "Holographic laser radar," *Opt. Lett.* **18**(5), 385–387 (1993).

8. J. C. Marron et al., "Atmospheric turbulence correction using digital holographic detection: experimental results," *Opt. Express* **17**(14), 11638–11651 (2009).

9. A. E. Tippie and J. R. Fienup, "Phase-error correction for multiple planes using a sharpness metric," *Opt. Lett.* **34**(5), 701–703 (2009)

10. A. E. Tippie and J. R. Fienup, "Multiple-plane anisoplanatic phase correction in a laboratory digital holography experiment," *Opt. Lett.* **35**(19), 3291–3293 (2010).

11. C. J. Pellizzari, M. F. Spencer, and C. A. Bouman, "Imaging through distributed-volume aberrations using single-shot digital holography," *J. Opt. Soc. Am. A* **36**(2), A20–A33 (2019).

12. C. J. Radosevich et al., "Imaging through deep turbulence using single-shot digital holography data," *Opt. Express* **28**(13), 19390–19401 (2020).

13. D. E. Thornton et al., "Digital holography efficiency measurements with excess noise," *Appl. Opt.* **58**(34), G19–G30 (2019).

14. D. E. Thornton et al., "Digital holography experiments with degraded temporal coherence," *Opt. Eng.* **59**(10), 102406 (2020).

15. D. E. Thornton et al., "Impacts of laboratory vibrations and laser flicker noise," *IEEE J. Quantum Electron.* **56**(5), 1400107 (2020).

16. D. E. Thornton et al., "Achieving the shot-noise limit using experimental multi-shot digital holography data," *Opt. Express* **29**(6), 9599–9617 (2021).

17. D. E. Thornton, M. T. Banet, and M. F. Spencer, "Subaperture sampling for digital-holography applications involving atmospheric turbulence," *Appl. Opt.* **60**(25), G30–G39 (2021).

18. S. A. Owens et al., "Pulsed laser source digital holography efficiency measurements," *Appl. Opt.* **61**(16), 4823–4832 (2022).

19. S. A. Owens, M. F. Spencer, and G. P. Perram, "Complex phase effects on a pulsed-source digital holography system," *Proc. SPIE* **12092**, 1209206 (2022).

20. P. M. Woodward, *Probability and Information Theory with Applications to Radar*, Artech House, Norwood, Maryland (1980).

21. L. G. Weiss, "Wavelets and wideband correlation processing," *IEEE Signal Process. Mag.* **11**(1), 13–32 (1994).

22. N. Levanon and E. Mozeson, *Radar Signals*, John Wiley & Sons, Inc., Hoboken, New Jersey (2004).

23. Coherent High Energy Pulsed Fiber Laser System (CHELS), *Product User Manual (6000456)*, NP Photonics (2020).

24. L. L. Steinmetz, W. A. Bookless, and J. H. Richardson, "Recent pulse width and linewidth measurements on the mode-locked Kr^+-ion laser," *Appl. Opt.* **19**(16), 2663–2665 (1980).

25. J. Xue et al., "Pulsed laser linewidth measurement using Fabry–Perot scanning interferometer," *Results Phys.* **6**, 698–703 (2016).

26. J. W. Goodman, *Statistical Optics*, 2nd ed., Wiley, Hoboken, New Jersey (2015).

27. A. Webster, *Useful Mathematical Formulas for Transform Limited Pulses*, Dover Publications, Mineola, New York (1964).

28. J. W. Goodman, *Introduction to Fourier Optics*, 4th ed., W. H. Freeman and Company, New York, New York (2017).

29. W. E. Martin and D. Milam, "Interpulse interference and passive laser pulse shapers," *Appl. Opt.* **15**(12), 3054–3061 (1976).

30. B. J. Davis, "Observable coherence theory for statistically periodic fields," *Phys. Rev. A* **76**(4), 043843 (2007).

31. R. W. Schoonover et al., "Optical interferometry with pulsed fields," *J. Mod. Opt.* **55**(10), 1541–1556 (2008).

32. Y. Liu et al., "Optimization methods of pulse-to-pulse alignment using femtosecond pulse laser based on temporal coherence function for practical distance measurement," *Opt. Lasers Eng.* **101**, 35–43 (2018).

33. R. Dutta et al., "Two-time coherence of pulse trains and the integrated degree of temporal coherence," *J. Opt. Soc. Am. A* **32**(9), 1631–1637, 2015.

Steven A. Owens received his BS degree in physics from the U.S. Air Force Academy in 2014 and his MS degree in engineering physics from the Air Force Institute of Technology (AFIT) in 2016. He is currently a PhD candidate at AFIT and is a student member of SPIE.

Mark F. Spencer is currently the directed energy staff specialist at Headquarters US Indo-Pacific Command as the first-ever liaison from the Air Force Research Laboratory at the Directed Energy Directorate. He is also an adjunct associate professor of optical sciences and engineering in the Department of Engineering Physics at the AFIT. He is a fellow of SPIE and is a senior member of Optica.

Glen P. Perram received his BS degree in applied and engineering physics from Cornell University in 1980 and his PhD in physics from AFIT in 1986. He has been a professor of physics at the AFIT since 1989. He is a fellow of the Directed Energy Professional Society and Optica. He is a registered professional engineer at the State of Ohio. He received the 2013 Air Force Outstanding Civilian Senior Scientist award for his work on Diode Pumped Alkali Lasers and the General Bernard A. Schriever award for advancing aerospace power in 1995.